

Supercritical fluids in porous composite materials: Direction-dependent flow properties

Mahnaz Firouzi, Muhammad Sahimi,* and Theodore T. Tsotsis

Department of Chemical Engineering and Materials Science, University of Southern California, Los Angeles, California 90089-1211, USA

(Received 18 August 2005; revised manuscript received 18 October 2005; published 24 March 2006)

The results of extensive nonequilibrium molecular dynamics simulations of flow and transport of a pure fluid, as well as a binary fluid mixture, through a porous material composed of a macropore, a mesopore, and a nanopore, in the presence of an external pressure gradient, are reported. We find that under supercritical conditions, unusual phenomena occur that give rise to *direction*-dependent and pressure-dependent permeabilities for the fluids' components. The results, which are also in agreement with a continuum formulation of the problem, indicate that the composite nature of the material, coupled with condensation, give rise to the direction-dependent permeabilities. Therefore, modeling flow and transport of fluids, in the *supercritical regime*, in porous materials with the type of morphology considered in this paper (such as supported porous membranes) would require using effective permeabilities that depend on both the external pressure drop and the direction along which it is applied to the materials.

DOI: [10.1103/PhysRevE.73.036312](https://doi.org/10.1103/PhysRevE.73.036312)

PACS number(s): 47.56.+r, 02.70.Ns

I. INTRODUCTION

Equilibrium and nonequilibrium properties of fluids and their mixtures in confined media are of much current interest [1,2]. Examples of such media include nanoporous and mesoporous materials, such as catalysts, adsorbents, skin and biological tissues, and nanoporous thin films that are used as low-dielectric constant composites, optical coatings, sensors, and insulating materials. For practical applications, it is important to understand how flow and transport processes occur in the pore space of such materials, because even if the properties of their matrix are of interest, understanding transport of fluids in their pore space is still critical to *characterization* of their morphology, including their matrix.

An important class of nanoporous materials consists of membranes—either biological or synthetic. The former play a fundamental role in biological activities of living organisms, while the latter, the focus of the present paper, are under active investigations, both experimentally and by computer simulations, for separation of fluid mixtures into their constituent components, and for sensors that can detect trace amounts of certain chemical compounds. Since molecular interactions between the fluid molecules, and between them and the nanopores' walls, cannot be ignored, one must resort to atomistic models [3]. Such models, that are typically based on atomistic simulation of flow and transport of a fluid mixture through a single nanopore, yield an effective permeability for each component of the mixture flowing through the nanopore. In practice, however, most membranes consist of a porous support made of at least two layers of macropores and mesopores, and a nanoporous film deposited on the support. Flow and transport of fluids in such composite porous materials have rarely been studied.

In this paper we report the results of the first atomistic simulation of flow and transport of supercritical (SC) fluid

mixtures—those that are in a thermodynamic state above their critical temperature and/or pressure—in a composite porous material that consists of three distinct pores, referred to as the macropores, mesopores, and nanopores. SC fluids have recently attracted much attention [4], due to the potential of SC fluid extraction (SCFE) utilizing CO₂ for removal of contaminants from water [5], sludges and soils [6], spent catalysts [7], aerogels [8], and adsorbents [9]. They are also used for preparing nanosize particles for drug delivery. CO₂ is preferred in such applications because it is nontoxic and nonflammable. The most promising SCFE method is one that combines a SC fluid with a porous membrane, which preferentially and continuously extracts the solute, leaving behind a solute-depleted, recyclable SC solvent stream. Experiments [10] indicate the existence of complex and unusual phenomena: hysteresis in the permeability isotherms at some temperatures but not at others; pressure-dependent permeabilities that exhibit a maximum as a function of the temperature, and solute rejection that can be positive or negative, depending on the type of the porous material and the solutes used. There is currently little fundamental understanding of such phenomena. We use molecular dynamics (MD) simulations to study flow and transport of a SC fluid mixture in a model composite membrane. In practice, a fluid mixture passes through a porous membrane by applying a pressure gradient to two opposing external surfaces of the membrane. To simulate this process we use the dual control-volume grand-canonical MD (DCV-GCMD) simulation technique which is most suitable for simulating transport processes in systems that operate under an external potential gradient. Due to their thermal/mechanical stability and versatility, carbon molecular-sieve membranes (CMSMs) have been used by many groups [11,12] in experimental studies involving separation of fluid mixtures. Thus, in this paper we utilize a model CMSM to carry out the MD studies. One goal of the paper is to understand the effects of the membrane structure, and the pressure gradient applied to the membrane, on the flow properties of the fluid mixture passing through the membrane.

*Corresponding author. Electronic address: moe@iran.usc.edu

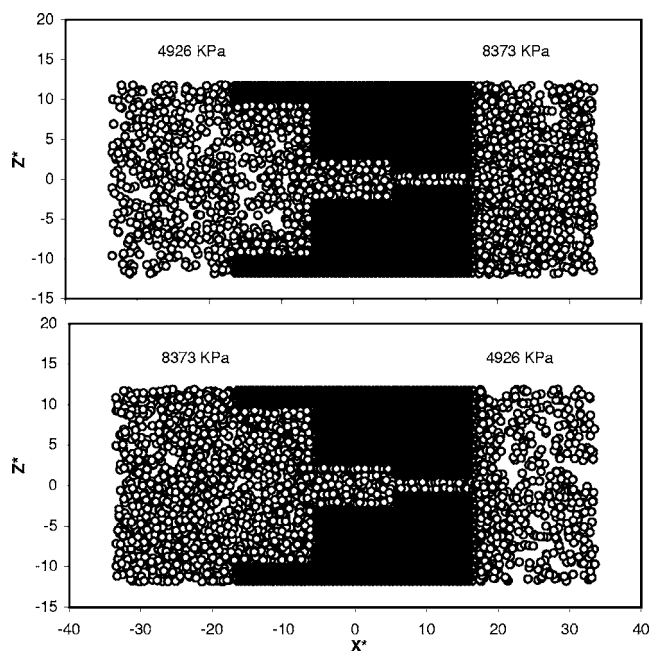


FIG. 1. A snapshot of the three-pore system and the distribution of pure CO₂ in it, when the upstream condition (higher pressure) is maintained either in the control volume which is connected to the macropore, or that connected to the nanopore.

The plan of this paper is as follows. In the next section we describe the details of the model of the membrane that we use and the MD simulation technique that we utilize. The results are presented and discussed in Sec. III. The paper is summarized in Sec. IV.

II. MOLECULAR DYNAMICS SIMULATION

Recent MD simulations [13] indicate that atomistic-scale transport in a pore is hardly influenced by the pore's shape. Thus, as a prelude to understanding flow and transport of SC fluid mixtures in a real membrane, we consider the same phenomena in the composite pore system shown in Fig. 1, which consist of three slit pores in series. (A somewhat similar pore model was utilized by Düren *et al.* [13] in their study of gas transport through a membrane.) Each pore represents one layer of a three-layer supported membrane. The pores' heights are 77, 23, and 10 Å, while they all have the same length, about 43 Å. The membrane is connected to two control volumes (CVs) that are exposed to the bulk fluid at high and low chemical potentials μ or pressures P . Periodic boundary conditions are used only in the y direction (perpendicular to the plane of this page). The external driving force is a chemical potential or pressure gradient applied in the x direction.

We consider flow and transport of pure CO₂, as well as a mixture of CH₄ (component 1) and CO₂ (component 2), in the membrane. The two components, as well as the carbon atoms that the pores' walls consist of, are represented by Lennard-Jones (LJ) spheres and are characterized by effective LJ size and energy parameters, σ and ϵ , respectively. We used $\sigma_C=3.4$ Å, and $\epsilon_C/k_B=28$ K for the carbon atoms; σ_1

$=3.81$ Å and $\epsilon_1/k_B=148.1$ K for CH₄, and $\sigma_2=3.79$ Å and $\epsilon_2/k_B=225.3$ K for CO₂. For the cross-term LJ parameters the Lorentz-Berthelot combining rules were used, namely, $\epsilon_{12}=\sqrt{\epsilon_1\epsilon_2}$, and $\sigma_{12}=\frac{1}{2}(\sigma_1+\sigma_2)$. We also used a more realistic model for CO₂ that consisted [14] of three LJ interaction sites on the three atoms, plus point charges to account for the quadrupole moment of CO₂ molecules, but found no significant effect on the results.

Although MD simulations have been used for studying SC fluids in the bulk [15], very few such studies have investigated the behavior of SC fluids in small pores [16,17]. As mentioned earlier, we use the DCV-GCMD method [14,18] which combines the MD method in the entire pore system with the grand-canonical Monte Carlo (GCMC) insertions and deletions of the molecules in the CVs. Therefore, to mimic the experimental conditions, the densities, or the corresponding chemical potentials, of the components in the CVs were maintained using a sufficient number of GCMC insertions and deletions. The probability of inserting a particle of component i is given by

$$p_i^+ = \min\left(\frac{Z_i V_c}{N_i + 1} \exp(-\Delta E/k_B T), 1\right), \quad (1)$$

where $Z_i = \exp(\mu_i/k_B T)/\Lambda_i^3$ is the absolute activity at temperature T , Λ_i , and μ_i are, respectively, the de Broglie wavelength and chemical potential of component i , ΔE the potential energy change resulting from inserting a particle, and V_c and N_i the volume of the CV and number of atoms of component i in each CV, respectively. The probability of deleting a particle is given by

$$p_i^- = \min\left(\frac{N_i}{Z_i V_c} \exp(-\Delta E/k_B T), 1\right). \quad (2)$$

The two CVs are well mixed and in equilibrium with the two bulk phases that are in direct contact with them. The chemical potentials were converted to equivalent pressures using a LJ equation of state [19].

The molecule-molecule interactions were modeled with the cut-and-shifted LJ 6-12 potential with a cutoff distance, $r_c=4\sigma_1$. To calculate the interactions between the fluids' molecules and the walls, we used the LJ potential for the interactions between the molecules and the individual carbon atoms on the walls, arranged as in graphite. The cutoff distance between the molecules and the carbon atoms on the walls was $r_c=3.5\sigma_1$. Typically, ten GCMC insertions and deletions in each CV were followed by one MD integration step. The temperature, $T=35$ °C, was held constant in order to eliminate any contribution of the temperature gradient to the transport.

The Verlet velocity algorithm was used to integrate the (dimensionless) equations of motion with a dimensionless time step, $\Delta t^*=5 \times 10^{-3}$ (i.e., $\Delta t \approx 0.00685$ ps). The equations of motion were integrated with up to 1.2×10^7 time steps to ensure that the system was at steady state. Molecules that crossed the outer boundaries of the CVs were removed. The number of such molecules was, however, small, typically about 1% of the total number of molecules that were deleted during the GCMC simulations. In addition, for each

component we allowed for a nonzero streaming velocity (the ratio of the component's flux and concentration) in the pore system, consistent with the presence of a bulk pressure/chemical potential gradient along the x direction. In the CVs, however, the overall streaming velocity was zero. Isokinetic conditions were maintained by rescaling the velocity independently in the three directions.

Two important quantities of interest are the density profile $\rho_i^z(x)$ of component i along the x direction, the direction along which the chemical potential gradient $\nabla\mu$ is imposed on the membrane, and $\rho_i^x(z)$, the density profile in the yz planes that are perpendicular to the direction of $\nabla\mu$. The density profile $\rho_i^z(x)$ was computed by dividing the simulation box in that direction into grids of size, $\ell=1.12\sigma_1$. For each MD step, $\rho_i^z(x)$ was computed by averaging the number of particles of type i over the distance ℓ . A similar procedure was used for computing the density profile $\rho_i^x(z)$ in the yz planes that are perpendicular to the direction of $\nabla\mu$, with the averaging done over a small distance which were about $0.67\sigma_1$, $0.21\sigma_1$, and $0.09\sigma_1$ for the macropores, mesopores, and nanopores, respectively.

In addition, a most important characteristic property of a membrane is the permeability of a fluid passing through the membrane. Thus, for each component i we calculated its flux J_i in the direction of the applied chemical potential or pressure gradient. The permeability K_i of the component i is then given by Darcy's law

$$K_i = \frac{J_i}{\Delta P_i/L}, \tag{3}$$

where $\Delta P_i=x_i\Delta P$ is the partial pressure drop for species i along the pore system, with x_i being its mole fraction, ΔP the total pressure drop imposed on the system, and L the system's length. We computed the permeabilities for two cases. In one, the upstream condition (higher pressure) was maintained in the CV connected to the macropore, while in the second case the upstream condition was maintained in the nanopore.

III. RESULTS AND DISCUSSION

We first describe the results for pure CO₂, and then present and discuss those for a binary mixture of CO₂ and CH₄. Figure 1 presents a snapshot of the pore system and the distribution of CO₂ molecules in it. The upstream and downstream pressures were 8373 kPa (1215 psi) 4926 kPa (715 psi), respectively. In both cases, the state of CO₂ in the nanopores and mesopores is liquidlike, caused by condensation. The state of CO₂ in the macropore, on the other hand, depends on where the upstream condition is maintained. If the upstream condition is maintained in the CV connected to macropore, then the CO₂ density in the pore is high almost everywhere, resembling a liquidlike state. If, on the other hand, the upstream condition is maintained in the CV connected to the nanopore, the CO₂ density in the macropore near its entrance to the mesopore is high, but decreases somewhat as one gets away from this region towards the CV on the left side of the figure. These are consistent with the

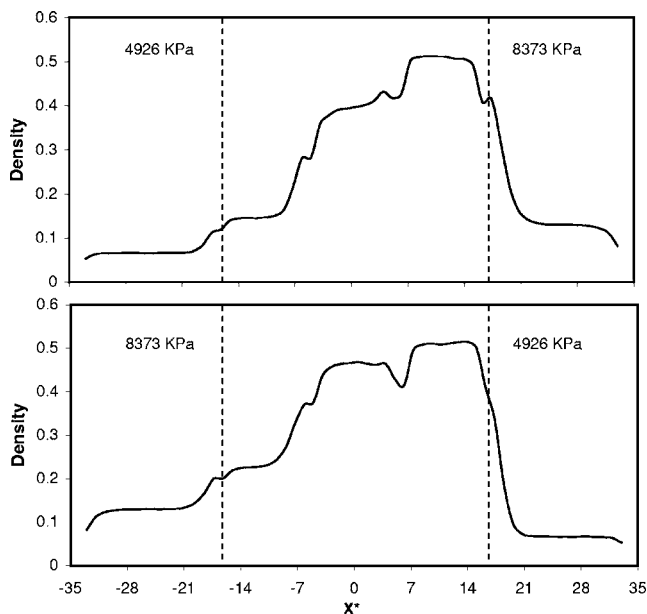


FIG. 2. Time-averaged density profiles $\rho^z(x)$ of pure CO₂ in the transport direction x . The system is at steady state.

time-averaged density profile $\rho^z(x)$ of CO₂ shown in Fig. 2.

Figure 3 presents the CO₂ permeabilities as a function of the upstream pressure, when a pressure drop $\Delta P=3447$ kPa (500 psi) was applied to the pore system. The direction dependence of K is striking, with the permeabilities in the two opposite directions differing by a factor which can be as large as nearly four. Moreover, the trends for the two cases are opposite of each other. Whereas K decreases when the upstream is on the macropore side, it increases when the direction of ΔP is reversed. The reason can be understood by considering Figs. 1 and 2: at a constant overall ΔP , with increasing the upstream pressure on the macropore side, practically the entire pore system is packed with CO₂ molecules. This makes the passage of the molecules from the macropore to the mesopore very difficult, resulting in reduced values of K . On the other hand, at the same overall ΔP , increasing the upstream pressure when applied on the

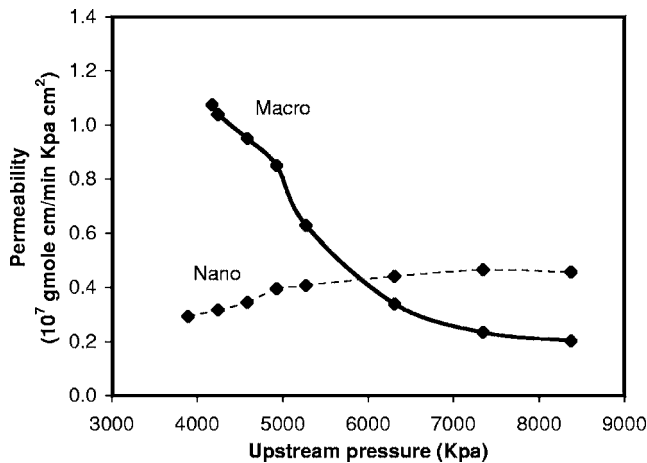


FIG. 3. The permeability of pure CO₂ when a pressure drop $\Delta P=3447$ kPa (500 psi) is applied to the pore system.

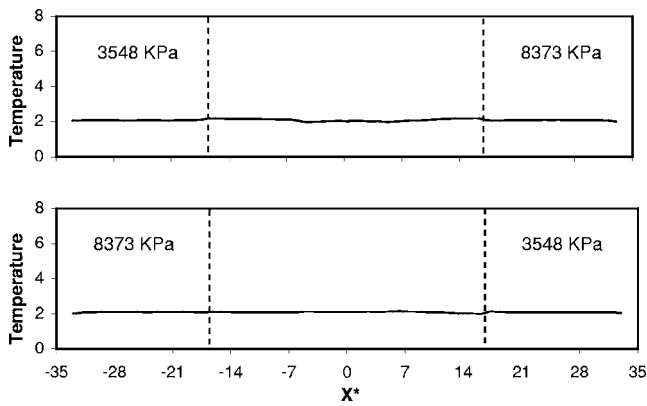


FIG. 4. Time-averaged temperature distribution in the pore system used in the simulation of the CO₂-CH₄ mixture.

nanopore side moves the transition point between a gaslike and liquidlike state to inside the macropore, hence making the passage of the molecules from the mesopore to the macropore easier, which increases K in that direction.

We now present the results for the binary mixture. Figure 4 shows the (dimensionless) temperature (averaged in the yz planes) throughout the pore system, which indicates that it remains constant. Hence, all the possible effects due to a temperature gradient have been eliminated. Figure 5 presents a snapshot of the pore system and the distribution of CO₂ and CH₄ molecules in it, after the steady state was reached, with the upstream and downstream pressures being 1215 psi (8373 kPa) and 515 psi (3548 kPa), respectively. To understand the distributions of the two molecules in the pores better, we present in Figs. 6 and 7 the time-averaged densities $\rho_i^x(z)$ for the two molecules at six different planes that are perpendicular to the direction of ΔP (the coordinates'

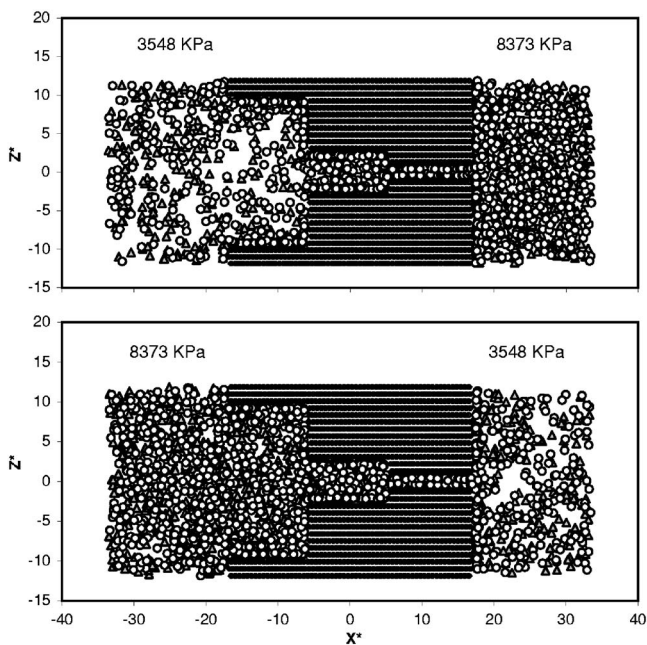


FIG. 5. A snapshot of the pore system with the distributions of CO₂ (circles) and CH₄ (triangles) in an equimolar mixture. The system is at steady state.

center is on the centerline that passes through the three pores). Figure 6 shows the density profiles when the upstream condition is maintained in the CV which is connected to the macropore. In plane 1 near the pore mouth connected to the CV, two layers of each type of molecule have been formed. One, with high densities, is near the walls, while the second one with lower densities is closer to the center. In the opposite plane (denoted by 2 in Fig. 6) near the macropore mouth that connects it to the mesopore, the density profiles look chaotic, with several layers of the two molecules forming. This is caused by the entrance effect whereby, due to the size of the mesopore which is much smaller than that of the macropore, a large number of molecules accumulates at the macropore's entrance to the mesopore. But, if we inspect the density profiles just inside the mesopore (denoted by 3 in the figure), we find again that two layers of each type of molecules have been formed inside the mesopore. The molecules' distributions in the region where the mesopore is connected to the nanopore (denoted by 4 in the figure) are qualitatively similar to those in plane 2, and are again dominated by the entrance effects. The very small size of the nanopore allows only monolayer formation. As a result, one obtains the density profiles shown in Fig. 6 for planes 5 and 6 shown in the figure. The same qualitative patterns are obtained when the upstream condition is held in the CV connected to the nanopore (see Fig. 7), but with one difference: Only one layer of each type of molecules has been formed in plane 1, where the macropore is connected to the CV. This is clearly caused by the low downstream pressure which gives rise to a gaslike state in that region, and is also consistent with the snapshot of the pore system shown in Fig. 5.

Figure 8 presents the time-averaged density profiles $\rho_i^z(x)$ of the two components (averaged in the yz planes) for the two upstream conditions. The mixture is equimolar. The densities in the two bulk regions are constant, as they should be. As one moves from the macropore to mesopore to nanopore, the densities, regardless of the direction of ΔP (or the upstream condition), increase since the pores' sizes decrease. A closer inspection of the densities in the pores indicates that, for the applied ΔP , one has a gaslike (low density) mixture in much of the macropore in both cases, followed by a transition to a liquidlike mixture (due to condensation) which packs the mesopores and nanopores completely at high densities. The position of the transition line from the gaslike to liquidlike mixture depends on the pores' sizes and the direction of ΔP . The density profiles shown in Fig. 8 are consistent with the snapshot of the system shown in Fig. 5, as they should be. At the same time, we should point out that, although we carried out long simulations, the slight increase in the density profile $\rho^z(x)$ of CO₂ (the dashed curve) in the nanopore, when the upstream condition is imposed on this pore (see the upper panel in Fig. 8), could still be due to nonequilibrium effects that may be exceedingly difficult to detect in our simulations.

Figure 9 presents the permeabilities of the two components in an equimolar mixture with $\Delta P=4825$ kPa (700 psi), computed when the pressure drop was applied in the two opposite directions shown in Figs. 1 and 5, and the upstream pressure was varied. The same qualitative patterns are obtained when other values of pressure drops are applied, and

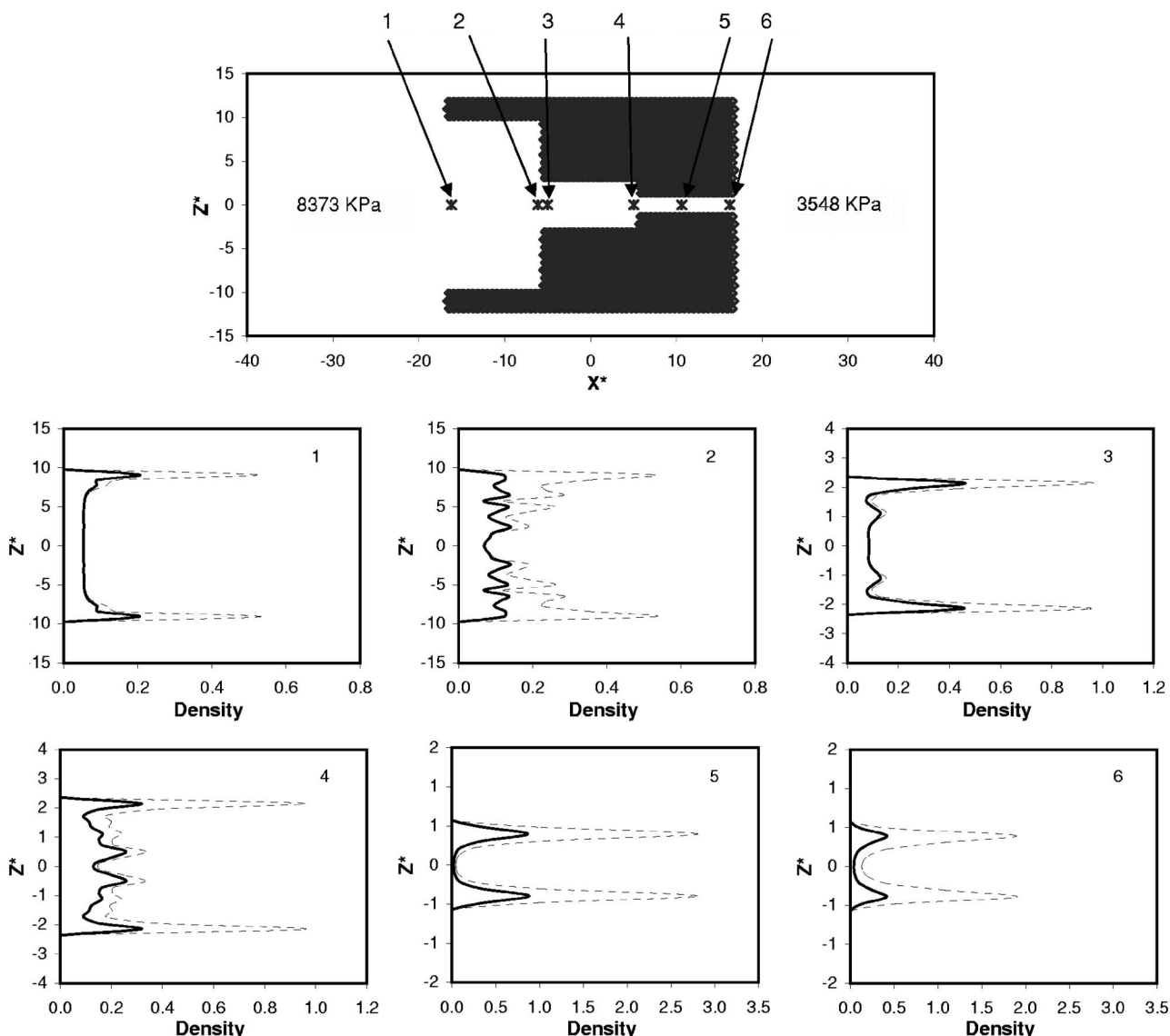


FIG. 6. Time-averaged density profiles $\rho_i^x(z)$ of CO₂ (dashed curves) and CH₄ (solid curves), when the upstream condition is maintained in the control volume connected to the macropore. The mixture is equimolar.

the upstream and downstream conditions are such that one crosses from a subcritical region to a supercritical one (the critical pressure for CO₂ is about 7380 kPa). In addition to the fact that the pressure dependence of K_1 and K_2 is in qualitative agreement with experimental data [10,20], another noteworthy feature of Fig. 9 is that the permeabilities differ significantly, with K_2 —that of CO₂—being larger. The reason is that, due to affinity of CO₂ for carbon surfaces, there is significant flow of CO₂ on or near the walls which is not the case for CH₄. This is particularly important, as the nanopores and mesopores are packed with molecules and, therefore, the molecules' motion in the bulk of the pores is exceedingly slow. Hence, surface flow becomes important.

The direction dependence of the permeabilities, for both pure CO₂ and those in the mixture, may be explained based on a continuum model. As is well known, transport in a macropore is dominated by convection, which gives rise to a permeability independent of the direction of the applied pres-

sure gradient. In a mesopore, transport is by a combination of convection and Knudsen diffusion [2,20], whereas in a nanopore, due to its small size and the condensation phenomenon, transport occurs mostly through surface flow. While condensation does play a role in the direction dependence of the effective permeabilities, the most important factor appears to be the composite nature of the system. To see this, we make an analogy between the resistances that the three pores in series offer against transport and that of electrical resistors. Then, because the three pores are in series, the effective permeability K_e of the pore system is given by

$$K_e = L \left[\sum_{i=1}^3 \left(\frac{K_i}{L_i} \right) \right]^{-1}, \tag{4}$$

where K_i and L_i are, respectively, the overall permeance and length of pore number i . It is now not difficult to show that it is the nonlinear dependence of K_e on K_i that is mostly re-

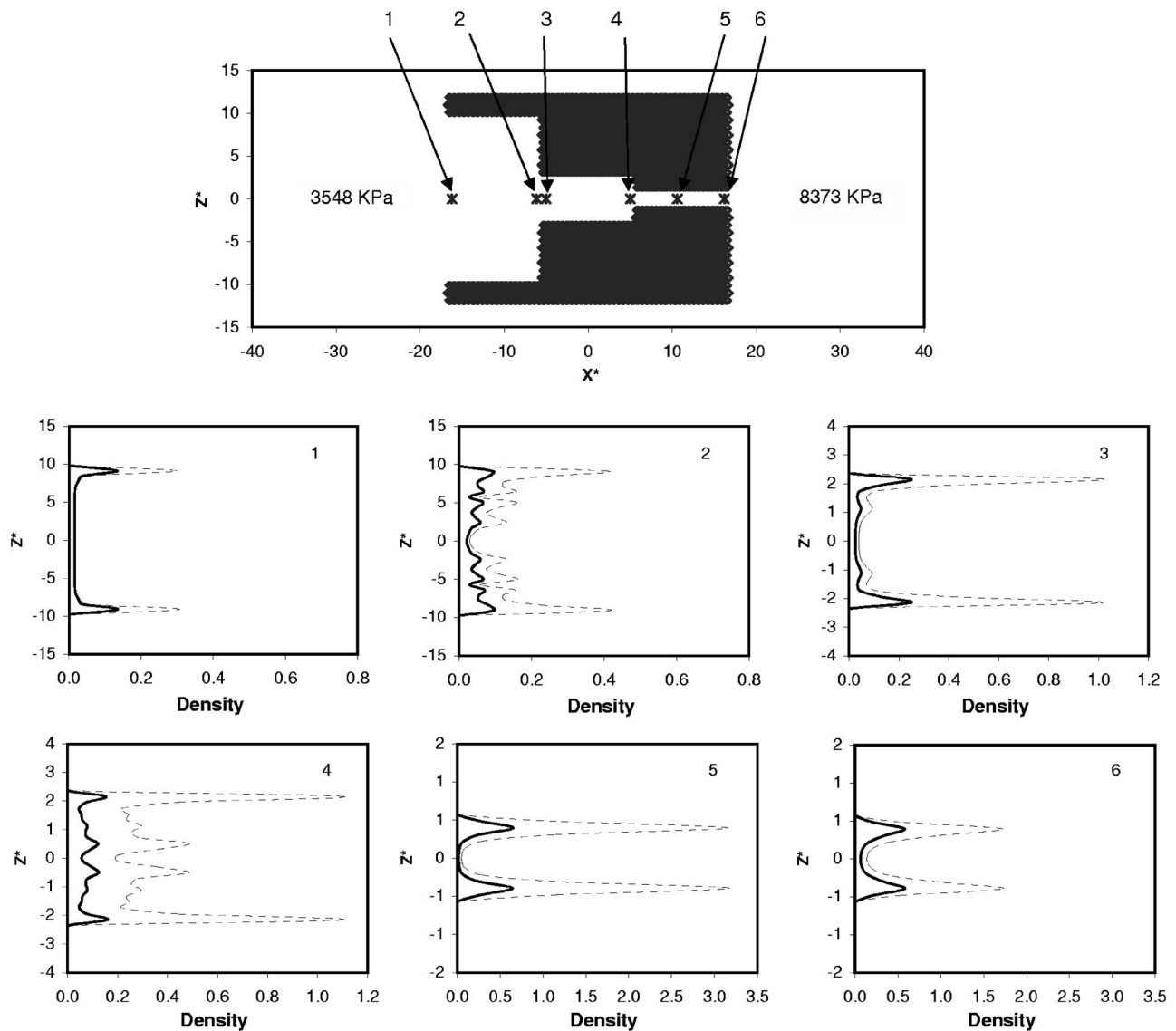


FIG. 7. Same as in Fig. 6, but when the upstream condition is maintained in the control volume connected to the nanopore.

responsible for its direction dependence. This is true even if one has a gaseous mixture in the composite pore system, as opposed to liquidlike mixtures (caused by condensation) that we deal with in our pore system. To show this, we proceed as follows.

Consider, first, transport of a gas in a single pore and assume that the gas is transported by a combination of convection and Knudsen diffusion. Hence, its flux is given by [2,20,21]

$$J = - \left(D_k \frac{dP}{dx} + K_p P \frac{dP}{dx} \right), \quad (5)$$

where D_k is the Knudsen diffusivity of the gas. K_p is a permeability coefficient defined for gases (according to Darcy's law, $K_p P$ is what is usually referred to as the permeability). K_p is independent of the pressure. Assuming, as usual, that D_k is also independent of the pressure, then, since the flux J

is constant at steady state, Eq. (4) can be easily integrated to yield

$$J = -L^{-1} \left[D_k (P_2 - P_1) + \frac{1}{2} K_p (P_2^2 - P_1^2) \right], \quad (6)$$

where P_1 and P_2 are the applied pressure at the pores' ends, and L is its length. According to Eq. (6), the magnitude of the flux and, therefore, the effective permeability K_e given by,

$$K_e = D_k + \frac{1}{2} K_p (P_1 + P_2), \quad (7)$$

are independent of the *direction* of the applied pressure drop, $\Delta P = P_2 - P_1$, because the interchanges, $P_1 \rightarrow P_2$ and $P_2 \rightarrow P_1$ would not alter Eq. (7). Note that, even if we replace the convective term of Eq. (5) by KdP/dx , which is the appropriate form for liquids and the liquidlike mixtures (such as those under supercritical conditions), the conclusion that in a *single pore* K_e does not depend on the direction of ΔP

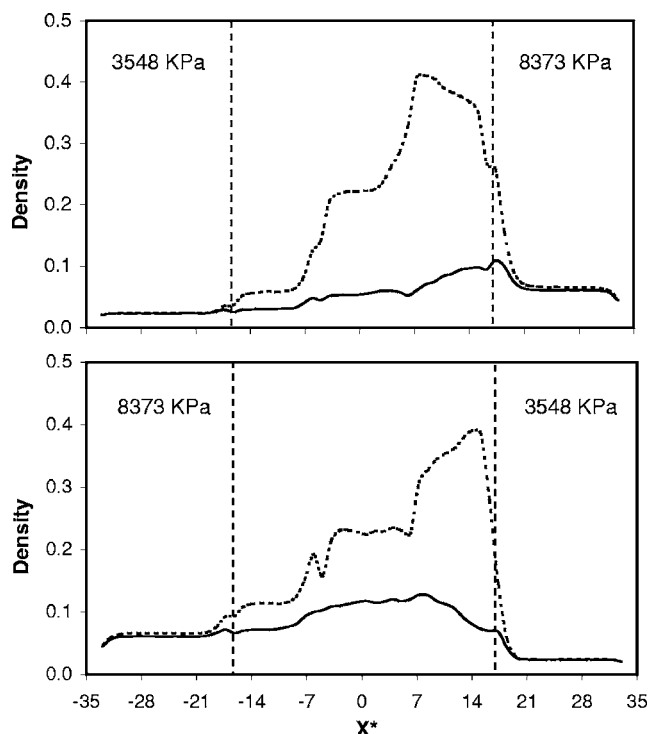


FIG. 8. Time-averaged density profiles $\rho_i^z(x)$ of CO₂ (dashed curves) and CH₄ (solid curves), in an equimolar mixture.

will remain true, since in that case, $K_e = D_k + \frac{1}{2}K$.

Next, consider two pores that are in series, and suppose that the pressure at the interface between them is P_i [21]. We assume that in one pore, say pore 1, convection is the dominant mechanism of transport (as in the macropore), while both convection and Knudsen diffusion contribute to transport in pore 2 (as in the mesopore). Hence, using Eq. (6), we write down the following expressions for the fluxes J_1 and J_2 in the two pores

$$J_1 = -\frac{1}{2}L_1^{-1}K_p^{(1)}(P_i^2 - P_1^2), \quad (8)$$

$$J_2 = -L_2^{-1} \left[D_k^{(2)}(P_2 - P_i) + \frac{1}{2}K_p^{(2)}(P_2^2 - P_i^2) \right]. \quad (9)$$

At steady state, $J_1 = J_2$. Therefore, we only need to determine the pressure P_i , which is obtained by requiring that, $J_1 = J_2$, yielding a second-order equation, $aP_i^2 + bP_i + c = 0$, in which the parameters a , b , and c are given by

$$a = \frac{1}{2}[\alpha K_p^{(1)} + K_p^{(2)}],$$

$$b = D_k^{(2)},$$

$$c = - \left[\frac{1}{2}\alpha K_p^{(1)}P_1^2 + \frac{1}{2}K_p^{(2)}P_2^2 + D_k^{(2)}P_2 \right], \quad (10)$$

where $\alpha = L_2/L_1$. It is now not difficult to see that the magnitude of the flux, $J = J_1 = J_2$, depends on the *direction* of ΔP by making the interchanges, $P_1 \rightarrow P_2$ and $P_2 \rightarrow P_1$, in agreement with the MD simulations presented above. Clearly, the same approach can be extended to the three-pore system we use in the simulations. Moreover, the conclusion will not change if, for example, Knudsen diffusion is the dominant transport mechanism in one pore, while convection contributes the most to the transport in another pore.

IV. SUMMARY

The results presented in this paper indicate the significance of the pore structure and the fluids' state to their transport through a porous material. In particular, aside from being in qualitative agreement with our preliminary experimental data [22], the results have two important implications:

(1) The classical modeling of transport of fluids through porous membranes, based on a single effective permeability independent of the direction of the applied pressure gradient, is inadequate if they have a composite structure similar to what we use in the present paper. This is usually the case when the membrane has a support structure.

(2) Unlike the popular practice, a single pore is a gross and inadequate model of an actual composite (supported) membrane, which typically consists of several layers, each characterized by their own morphological and transport properties [21].

In practice, supercritical fluid extraction using CO₂ is utilized when the mixture contains heavier hydrocarbons, such as pentane and hexane. In such cases, the molecular structure of the hydrocarbons and their motion through the nanopores give rise to additional complexities, such as *freezing* phenomena whereby the mixture does not move appreciably even over long periods of times. Molecular dynamics simulation of flow and transport of such mixtures through the pore system considered in this paper is underway. The results will be reported in a future paper [23].

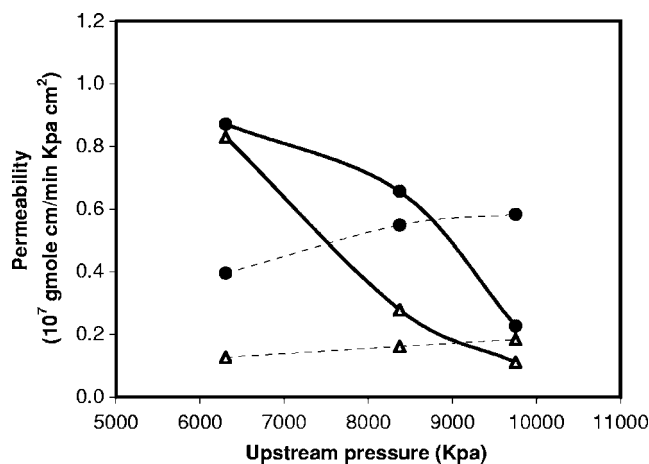


FIG. 9. The dependence of the permeabilities of CO₂ (circles) and CH₄ (triangles) on the upstream pressure, when a pressure drop, $\Delta P = 4825$ kPa (700 psi), is applied in the two opposite directions. Continuous and dashed curves show, respectively, the results when the upstream pressure is maintained at entrance to the macropore and nanopore.

ACKNOWLEDGMENTS

We are grateful to the National Science Foundation, the Department of Energy, the Petroleum Research Fund admin-

istered by the American Chemical Society, and Media and Process Technology, Inc., for partial support of this work. We would also like to thank the San Diego Supercomputer Center for providing much needed computer time.

-
- [1] *Access in Nanoporous Materials*, edited by T. J. Pinnavaia and M. F. Thorpe (Plenum, New York, 1995).
- [2] M. Sahimi, *Rev. Mod. Phys.* **65**, 1393 (1993); *Flow and Transport in Porous Media and Fractured Rock*, 2nd ed. (VCH, Weinheim, 2006); S. Torquato, *Random Heterogeneous Materials* (Springer, New York, 2002).
- [3] M. Sahimi and T. T. Tsotsis, in *Handbook of Computational Nanotechnology*, edited by W. Schommer and M. Reith (American, New York, 2005), Chap. 74; M. Sahimi, *Heterogeneous Materials II* (Springer, New York, 2003), Chap. 9.
- [4] E. Kiran and J. M. H. L. Sengers, *Supercritical Fluids-Fundamentals for Applications* (Kluwer, Dordrecht, 1994).
- [5] R. K. Roop *et al.*, *J. Supercrit. Fluids* **1**, 31 (1988); Y. Meguro *et al.*, *Radiochim. Acta* **75**, 185 (1996).
- [6] M. H. Liu *et al.*, *Chemosphere* **23**, 1088 (1991); A. Firus, W. Weber, and G. Brunner, *Sep. Sci. Technol.* **32**, 1403 (1997).
- [7] L. J. Silva, L. A. Bray, and D. W. Matson, *Ind. Eng. Chem. Res.* **32**, 2485 (1993).
- [8] Z. Novak and Z. Knez, *J. Non-Cryst. Solids* **221**, 163 (1997); P. Wawrzyniak *et al.*, *ibid.* **225**, 86 (1998).
- [9] D. L. Tomasco *et al.*, *Environ. Prog.* **12**, 208 (1993); D. L. Tomasco *et al.*, *Sep. Sci. Technol.* **30**, 1901 (1995).
- [10] H. Ohya *et al.*, *J. Membr. Sci.* **84**, 185 (1993); S. Sarrade, G. M. Rios, and M. Carles, *ibid.* **114**, 81 (1996); Y. Tokunaga, T. Fujii, and K. Nakamura, *J. Card. Surg.* **61**, 1024 (1997).
- [11] V. M. Linkov, R. D. Sanderson, and E. P. Jacobs, *Mater. Lett.* **20**, 43 (1994); T. Steriotis *et al.*, *J. Appl. Polym. Sci.* **64**, 2323 (1997); M. B. Shiflett and H. C. Foley, *Science* **285**, 1902 (1999).
- [12] M. G. Sedigh, W. J. Onstot, L. Xu, W. L. Peng, T. T. Tsotsis, and M. Sahimi, *J. Phys. Chem. A* **102**, 8580 (1998); M. G. Sedigh, L. Xu, T. T. Tsotsis, and M. Sahimi, *Ind. Eng. Chem. Res.* **38**, 3367 (1999); M. G. Sedigh, M. Jahangiri, P. K. T. Liu, M. Sahimi, and T. T. Tsotsis, *AIChE J.* **46**, 2245 (2000).
- [13] T. Düren, S. Jakobtorweihen, F. J. Keil, and N. A. Seaton, *Phys. Chem. Chem. Phys.* **5**, 369 (2003).
- [14] L. Xu, M. G. Sedigh, M. Sahimi, and T. T. Tsotsis, *Phys. Rev. Lett.* **80**, 3511 (1998); L. Xu, M. G. Sedigh, T. T. Tsotsis, and M. Sahimi, *J. Chem. Phys.* **112**, 910 (2000); L. Xu, T. T. Tsotsis, and M. Sahimi, *ibid.* **111**, 3252 (1999); L. Xu, M. Sahimi, and T. T. Tsotsis, *Phys. Rev. E* **62**, 6942 (2000).
- [15] S. T. Chung and K. S. Shing, *Fluid Phase Equilib.* **81**, 321 (1992); C. A. Eckert, B. L. Knutson, and P. G. Debenedetti, *Nature (London)* **383**, 313 (1996); A. A. Chialvo and P. T. Cummings, *Adv. Chem. Phys.* **109**, 115 (1999).
- [16] D. Nicholson, *Carbon* **36**, 1511 (1998); T. Shingetta, J. Yoneya, and T. Nitta, *Mol. Simul.* **16**, 291 (1996); G. K. Papadopoulos, *J. Chem. Phys.* **114**, 8139 (2001).
- [17] M. Firouzi, T. T. Tsotsis, and M. Sahimi, *J. Chem. Phys.* **119**, 6810 (2004).
- [18] G. S. Heffelfinger and F. van Swol, *J. Chem. Phys.* **100**, 7548 (1994); R. F. Cracknell, D. Nicholson, and N. Quirke, *Phys. Rev. Lett.* **74**, 2463 (1995); D. M. Ford and G. S. Heffelfinger, *Mol. Phys.* **94**, 673 (1998).
- [19] J. K. Johnson, J. A. Zollweg, and K. E. Gubbins, *Mol. Phys.* **78**, 591 (1993).
- [20] E. Mason and A. P. Malinauskas, *Gas Transport in Porous Media: The Dusty Gas Model* (Elsevier, Amsterdam, 1983).
- [21] P. Uchytíl, O. Schramm, and A. Seidel-Morgenstern, *J. Membr. Sci.* **170**, 215 (2000); S. Thomas, R. Schäfer, J. Caro, and A. Seidel-Morgenstern, *Catal. Today* **67**, 205 (2001).
- [22] Kh. Molaai Nezhad, M. Sahimi, and T. T. Tsotsis (unpublished).
- [23] M. Firouzi, T. T. Tsotsis, and M. Sahimi (unpublished).